Journal of Hazardous Materials 438 (2022) 129438

Contents lists available at ScienceDirect

Journal of Hazardous Materials

journal homepage: www.elsevier.com/locate/jhazmat

In-situ constructed 2D/2D $ZnIn_2S_4/Bi_4Ti_3O_{12}$ S-scheme heterojunction for degradation of tetracycline: Performance and mechanism insights

Qi Zhou, Luhong Zhang, Longfei Zhang, Bin Jiang, Yongli Sun *

School of Chemical Engineering and Technology, Tianjin University, Tianjin 300072, People's Republic of China

HIGHLIGHTS

- The 2D/2D $ZnIn_2S_4/Bi_4Ti_3O_{12}$ S-scheme heterojunction was constructed.
- The photocatalyst showed high photocatalytic activity for TC degradation.
- The photocatalytic mechanism was confirmed by work function calculation.
- Built-in electric field enabled effective migration and separation of carriers.
- Possible degradation pathways and toxicity assessments were investigated.

GRAPHICAL ABSTRACT

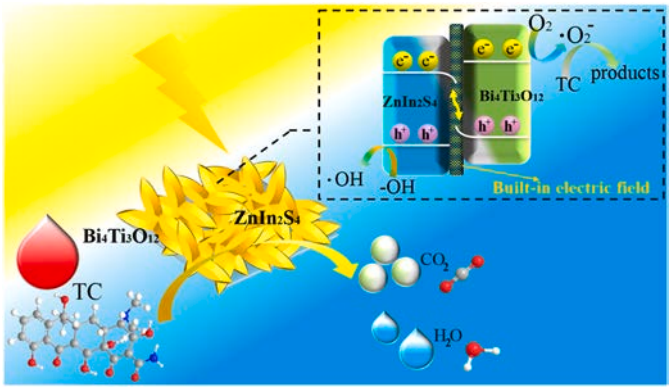

ARTICLE INFO

Editor: Sungjun Bae

Keywords:
Visible-light Photocatalysis
S-scheme heterojunction
2D/2D structure
Antibiotic removal
Water purification

ABSTRACT

Semiconductor materials dominated photocatalytic technology is one of the most efficient approaches to degrade organic pollutants. However, the limited light absorption range and rapid recombination of photogenerated carriers greatly restrict the application of photocatalysts. Rational design of photocatalysts to achieve high catalytic activity and stability is of great importance. Herein, $ZnIn_2S_4/Bi_4Ti_3O_{12}$ S-scheme heterojunction is synthesized by growing the $ZnIn_2S_4$ nanosheets on the sheet-like $Bi_4Ti_3O_{12}$ surface via a low-temperature solvothermal method. The TC removal efficiency of optimized heterojunction reaches 82.1% within 60 min under visible light, and the rate constant is nearly 6.8 times than that of pristine $ZnIn_2S_4$. The favorable photocatalytic performance of heterojunction is attributed to the tight contact interface and efficient separation of photogenerated carriers. Besides, the difference in work function between $ZnIn_2S_4$ and $Bi_4Ti_3O_{12}$ leads to band bending and the establishment of built-in electric field on the contact interface of heterojunction, which facilitates the migration and separation of photogenerated carriers. Furthermore, the cycling test demonstrates the attractive stability of heterojunction. The possible TC photodegradation pathways and toxicity assessment of the intermediates are also analyzed. In conclusion, this work provides an effective strategy to prepare S-scheme heterojunction photocatalysts with favorable photocatalytic activity, which can enhance wastewater purification efficiency.

* Correspondence to: School of Chemical Engineering and Technology, Tianjin University, Tianjin 300072, China.
E-mail address: sunyongli@tju.edu.cn (Y. Sun).

https://doi.org/10.1016/j.jhazmat.2022.129438
Received 28 April 2022; Received in revised form 12 June 2022; Accepted 19 June 2022
Available online 21 June 2022

1. Introduction

Water pollution caused by pharmaceutical and agricultural pollutants has attracted widespread concern. Indiscriminate use of antibiotics seriously deteriorates the safety of human drinking water and the balance of aquatic ecosystem (Dou et al., 2022). Tetracycline hydrochloride (TC) as a typical antibiotic medicine has been widely used in aquaculture and animal husbandry to ease and prevent bacterial infection (Koutavarapu et al., 2022). However, TC shows a low metabolic rate in living organisms and higher water solubility (Li et al., 2022f). Hence, the problem of antibiotic residues is always inevitable, which will lead to kidney disease and induce the generation of antibiotic resistance genes. Conventional wastewater purification methods include coagulation, biological, and adsorption method cannot achieve effective treatment of antibiotics (Lian et al., 2022; Liu et al., 2020). Therefore, exploring a high degradation efficiency method to purify antibiotics-contaminated water is of great importance (Liu et al., 2022a).

The photocatalytic technology based on semiconductor materials has been considered as a simple and efficient strategy to solve environmental pollutants through oxidation or reduction reactions (Chen et al., 2022; Dou et al., 2022). Among all semiconductor photocatalysts, $Bi_4Ti_3O_{12}$ (BTO), an Aurivillius phase perovskite, is widely concerned due to its nontoxicity, safety, and good chemical stability (Wang et al., 2020). BTO has a unique layered crystal and the sandwich structure consisting of $(Bi_2Ti_3O_{10})^{2-}$ perovskite-type layer and alternating $(Bi_2O_2)^{2+}$ fluorite-type layers along the c-axis (Zhang et al., 2021). However, a series of shortcomings greatly limit the practical application of BTO. Like other photocatalysts, the photocatalytic activity of the pristine BTO is still unsatisfactory, which can be related to the fast recombination rate of photogenerated carriers. Besides, BTO performs a wide electronic bandgap (Eg = 2.9 eV) and is less effective for visible light utilization (Wang et al., 2020). To enhance the photocatalytic activity of the catalysts, several methods have been proposed, such as element doping, composite heterojunction, and noble metal deposition (Guo et al., 2016). The heterojunctions consisting of two or more semiconductors can facilitate photocatalytic activity by efficiently transporting and separating photogenerated electron-hole (e^--h^+) pairs (Jin et al., 2022).

Recently, the construction of step-scheme (S-scheme) heterojunction has been regarded as a research hotspot (Dai et al., 2022). In general, S-scheme heterojunction consists of two n-type semiconductors, and the coupling of the materials can preserve effective e^--h^+ and recombine meaningless photogenerated carriers to maintain maximal redox capacity (Jin et al., 2022; Wang et al., 2022a). The occurrence of band bending and the establishment of built-in electric field (IEF) are crucial to the migration and separation of photogenerated carriers on the contact interface of S-scheme heterojunction (Xu et al., 2021). Typically, Liu et al. proposed $Ag_3PO_4/Bi_4Ti_3O_{12}$ S-scheme heterojunctions with high degradation efficiency (78.2%) for the treatment of sulfamethoxazole, which was nearly 1.3 times that of the pure Ag_3PO_4 (Liu et al., 2020). The $Ag_3PO_4/Bi_4Ti_3O_{12}$ composite has a large specific surface area and shows low charge recombination efficiency due to the construction of S-scheme heterojunction. Therefore, the BTO is selected as a substrate to reasonably construct S-scheme heterojunction can obtain the high photocatalytic activity.

It's worth noting that, the surface morphology and structure feature are also the key criterion affecting the catalytic activity of photocatalysts (Wang et al., 2021). Both the diffusion distance of the photogenerated carrier and the number of the catalytic active sites are affected by the material structure and morphology (Zou et al., 2020). Theoretically, the 2D/2D composites not only show a larger specific surface area but also have a tighter face-to-face interfacial contact, thereby providing abundant electromigration channels and more exposed catalytic active sites (Wang, Y. et al., 2022; Zhao et al., 2021). More importantly, the construction of 2D/2D structure can short the migration path of photogenerated e^--h^+ from the interior to the surface and prolong the lifetime of photogenerated e^--h^+, which is decisive for the separation ability and migration efficiency of photogenerated carriers (Zhang et al., 2021). Therefore, the construction of 2D/2D structure is an effective method to enhance photocatalytic activity (Mu et al., 2022).

$ZnIn_2S_4$ (ZIS), as an important 2D n-type semiconductor photocatalyst, stands out for its simple operation, mild synthesis condition, and good optical property as well as excellent chemical stability (Xi et al., 2021). Moreover, ZIS has a high visible light absorption ability due to its narrow bandgap (2.35 eV). The layered ZIS not only has a high photoelectric conversion efficiency but also has a suitable redox potential (Tan et al., 2021). It has been widely applied in the pollutant degradation (Li et al., 2022f; Wang et al., 2022b). In particular, single-phase metal sulfide nanosheets are always agglomerated to form bulky aggregates, which exhibit low catalytic activity and instability (Fan et al., 2022; Wang et al., 2019). The structure of the original ZIS exhibits a flower-like hierarchical microsphere morphology consisting of some stacked nanosheets (Tan et al., 2021). Therefore, combining the suitable substrates and metal sulfide nanosheets to build the heterojunction can not only prevent the aggregation phenomenon but also enhance the photocatalytic activity. Wang et al. fabricated S-Scheme TiO_2 @$ZnIn_2S_4$ photocatalyst, the catalytic activity of heterojunction is increased by 4.43 times compared with pristine TiO_2, which depends on the S-scheme charge transfer mechanism to improve carrier separation and migration efficiency (Wang et al., 2021). Wang et al. synthesized S-scheme $ZnIn_2S_4/Bi_3TaO_7$ heterojunction to investigate the photodegradation of TC, the removal efficiency is nearly 3.8 times that of the single Bi_3TaO_7. The in situ XPS analysis and DFT reveal that the IEF and bent bands of S-scheme heterojunctions is the key to enhance catalytic activity (K. Wang et al., 2022; A. Wang et al., 2022; C. Wang et al., 2022; Y. Wang et al., 2022). Jin et al. designed WO_3 @$ZnIn_2S_4/Bi_2S_3$ heterojunction to achieve efficient elimination of Cr (VI) in wastewater. The Cr (VI) reduction efficiency was about 8.09 times higher than that of the raw material due to its larger surface area, numerous active sites and suitable carrier transport channels by the heterojunction (Jin et al., 2022). Meanwhile, the existence of IEF by S-scheme heterojunction can accelerate electron transfer to reduce the accumulation of photogenerated charges within the semiconductor, thereby reducing the harm of photo-corrosion (Jiang et al., 2021). Therefore, the introduction of ZIS to design 2D/2D heterojunction is an important strategy to improve the catalytic activity.

Herein, we present the molten salt method and low-temperature solvothermal method to fabricate 2D/2D ZIS/BTO S-scheme heterojunctions for visible light-driven photocatalytic degradation of TC. It can be foreseen that the ZIS/BTO composite integrates 2D/2D structure features and S-scheme heterojunction, which not only generate abundant active sites but also promote the separation of photogenerated e^--h^+. The surface morphology, chemical composition, and photoelectrochemical properties of the ZIS/BTO heterojunctions are investigated and analyzed. More importantly, the possible S-scheme carrier transfer mechanism has also been explored through band structure analysis, trapping experiment, ESR, and work function calculation. This work offers an effective strategy to fabricate S-scheme heterojunction photocatalysts, which shows a promising perspective for the application of photocatalytic antibiotics removal.

2. Experimental

2.1. Materials

Glycerol (98%), zinc acetate ($Zn(Ac)_2$, 99.5%), indium (III) chloride tetrahydrate ($InCl_3.4\ H_2O$, 98%), thioacetamide (CH_3CSNH_2, TAA, AR), bismuth (III) oxide (Bi_2O_3, 99%) were obtained from the Heowns Science And Technology Co. Ltd. (Tianjin, China). Titanium oxide (TiO_2, 99.8%) was purchased from Macklin Reagent Co. Ltd. (Shanghai, China). Sodium chloride and potassium chloride were provided by Tianli Chemicals Co. Ltd. (Tianjin, China). All chemicals were directly

used and without further purification.

2.2. Preparation method of BTO

Molten salt method was selected to prepare 2D BTO nanoplates. Initially, 1.86 g Bi_2O_3 and 0.48 g TiO_2 were milled for 10 min. Then, a certain proportion of KCl and NaCl (molar ratio of Bi_2O_3: TiO_2: KCl: NaCl= 2:3:50:50) were sequentially added and milled for 1 h. Afterward, the mixtures were calcined at 800 °C for 120 min and the heating rate was 5 °C/min. After cooling, the synthesized white samples were washed repeatedly by deionized water to separate the residual salts and dried overnight.

2.3. Preparation method of ZIS / BTO heterojunction

The in-situ growth of layered ZIS on the surface of the BTO nanoplates is achieved by the low-temperature solvothermal method (Fig. 1). Typically, 0.06 g of BTO was uniformly dispersed in the mixture solution contains 70 mL deionized water and 10 mL glycerol under 1 h ultrasonic treatment. After that, the precursors of ZIS including 0.36 g of $Zn(Ac)_2$, 0.4 g of $InCl_3$, and 0.3 g of TAA were sequentially dissolved in the above solution (pH = 2.5, adjusted by 0.5 M HCl) under vigorous stirring. Subsequently, the obtained mixture solution was transferred to a 150 mL round-bottom flask and moved into an oil bath at 80 °C for 4 h. Finally, the synthesized solid products were collected by centrifugation and washed repeatedly by deionized water and ethanol. After drying at 60 °C overnight, ZIS/BTO-40 was obtained. The different weight ratios of ZIS/BTO (1:0.3 and 1:0.5) heterojunctions were also synthesized. Simplicity, the samples were labelled as ZIS/BTO-30 and ZIS/BTO-50, respectively. In addition, the reaction procedure without adding BTO can obtain pure ZIS samples.

2.4. Characterization

The surface morphologies and microstructure of synthesized samples were characterized by scanning electron microscopy (SEM) (Hitachi S-4800) and transmission electron microscopy (TEM) (JEM-F200). The distribution of the elements was investigated by the energy dispersive spectrometer (EDS) using Hitachi S-4800 as well. The crystal phase and crystallinity of the sample were measured by X-ray diffraction (XRD) (Bruker, D8 Advance) in the 2θ range of 5–80°. The pore size, pore volume, and specific surface area were tested by the Brunauer-Emmett-Teller (BET) (Micromeritics ASAP 2460). The UV–vis spectrophotometer (UV-4802S, Unico) was selected to analyze the concentration of TC solution. The X-ray photoelectron spectroscopy (XPS) (Thermo ESCALAB 250Xi) was applied to obtain the elemental composition and valence state of material. Furthermore, the high-performance liquid chromatography-tandem mass spectrometry (Thermo Vanquish UHPLC-LTQ XL) was selected to analyze the intermediate products of the degradation process. The UV–vis diffuse reflectance spectroscopy (DRS) was performed on spectrometer (Shimadzu UV-3600). The Mott−-Schottky, transient photocurrent test, and electrochemical impedance spectroscopy (EIS) analysis were performed on the CHI660E electrochemistry workstation (Shanghai Chenhua Instrument Co. Ltd). The active oxygen species were monitored by the electron spin resonance (ESR) (Bruker EMX).

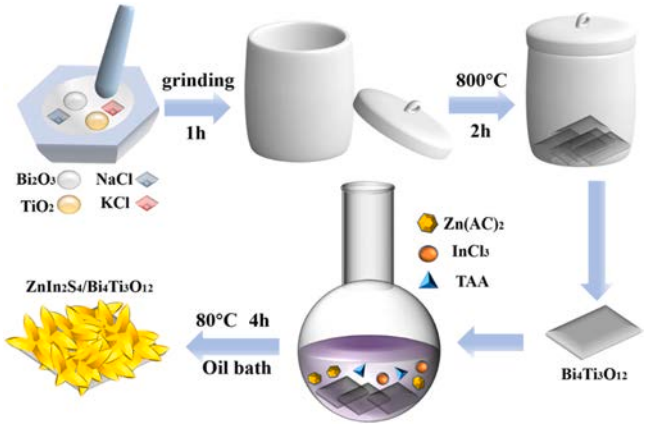

Fig. 1. Schematic illustration for the fabrication of ZIS/BTO.

2.5. Photocatalytic performance evaluation

The photocatalytic experimental box was selected to initiate the photodegradation experiments. A 300 W Xenon lamp with a 420 nm filter was served as the light source. To achieve a constant temperature during the degradation process, the condensate water needs to be kept circulating. Typically, 10 mg of as-prepared catalyst was added to the TC solution (20 ppm, 50 mL). Noticeably, the mixing system should be stirred for 30 min in darkness to realize adsorption equilibrium between catalysts and pollutants (Koutavarapu et al., 2022). After that, the Xenon lamp was turned on to achieve visible light irradiation. About 3–4 mL of suspension was sampled at a certain time interval and filtered by a 0.22 μm filter. Meanwhile, the TC concentration at different time intervals can be investigated by the UV–vis spectrophotometer at 357 nm. The removal efficiency (γ) is analyzed and calculated by Eq. (1).

$$\gamma = \left(1 - \frac{C_i}{C_0}\right) \times 100\% \quad (1)$$

where C_0 and C_i represent the TC concentrations of the original mixture and after light irradiation at different time intervals, respectively.

The reusability and stability of photocatalysts were investigated by cycling experiments. The experimental procedure was similar to the photodegradation experiment, except that catalyst was centrifuged, washed, and dried after the photodegradation process, and then the same process was repeated for 4 times.

2.6. Capturing of active oxygen species

The isopropanol (IPA), benzoquinone (BQ), and ammonium oxalate (AO) were regarded as trapping agents to capture hydroxyl radical (·OH), superoxide radical ($\cdot O_2^-$), and holes (h^+) during the photocatalytic processes, respectively.

3. Results and discussion

3.1. Morphology and microstructure of samples

The surface morphology and element distribution of samples are characterized in Fig. 2. In Fig. 2a, the BTO particles are of sheet-like shape, with a relatively smooth surface and the thickness of ca 100 nm (Fig. S1). Fig. 2b reveals that the structure of the original ZIS exhibits a flower-like hierarchical microsphere morphology consisting of some stacked nanosheets. As shown in Fig. 2c, the abundant ZIS petal-like nanosheets uniformly and tightly cover the surface of BTO, forming a 2D/2D structure. Notably, some stacked nanosheets may cause variation in nanoplate thickness and size of ZIS/BTO, and the sheet-like outline of BTO nanoplate can still be observed, which indicates the structure of BTO is not damaged after solvothermal treatment (Fig. S2). During the solution environment at pH = 2.5, the surface of the BTO exhibits positive charge (Fig. S3). Meanwhile, TAA is decomposed in acidic aqueous solutions and the negatively charged S^{2-} ions are released, which can be adsorbed on the outer surface of BTO nanoplates by electrostatic interactions. After that, the In^{3+} and Zn^{2+} cations could react with negative S^{2-} ions adhered on the BTO surface. Ultimately, abundant ZIS nanosheets are tightly anchored on the surfaces of BTO

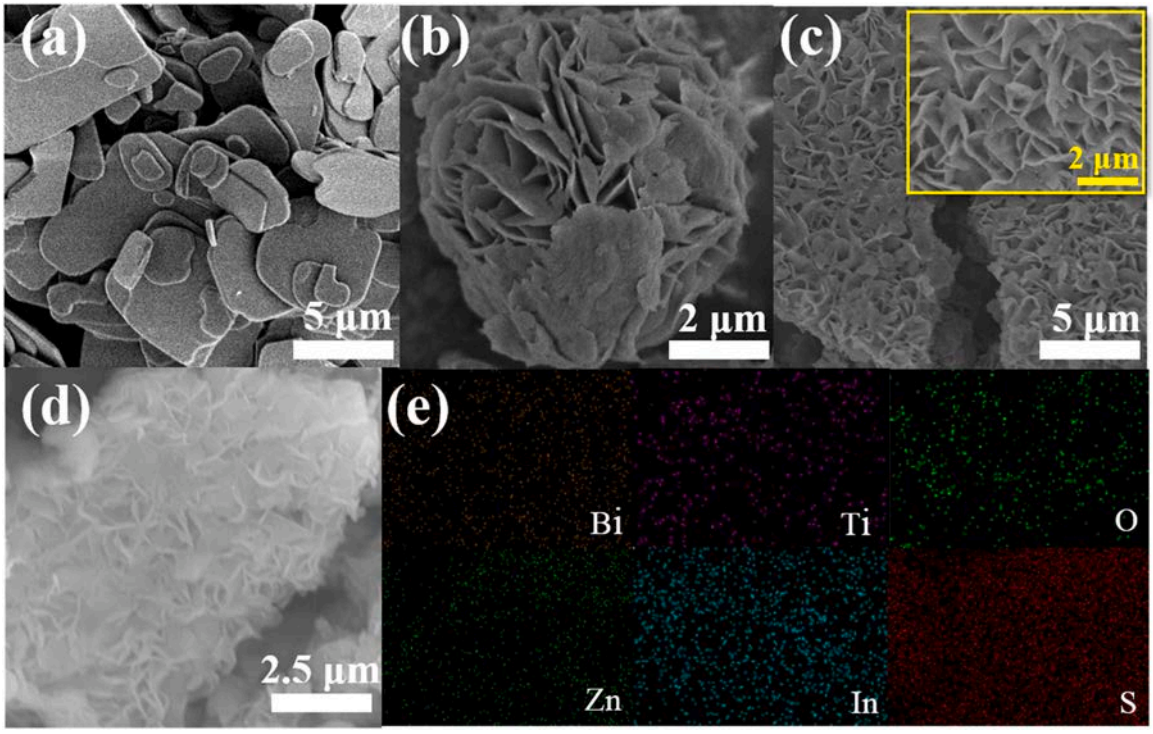

Fig. 2. SEM of (a) BTO, (b)ZIS, (c) ZIS/BTO. (d-e) elemental mapping images of ZIS/BTO.

nanoplates to obtain 2D/2D ZIS/BTO composites.

Additionally, the EDS mapping is selected to further investigate the distribution and content of each element on ZIS/BTO composite. As shown in Fig. 2d-e and Fig. S4, the element of Bi, Ti, O, Zn, In, and S are evenly distributed, demonstrating the successful synthesis of ZIS/BTO composites.

TEM is also employed to clearly identify structure and heterojunction of ZIS/BTO. As shown in Fig. 3a, the abundant ZIS nanosheets are distributed uniformly on the surface of sheet-like BTO. In Fig. 3b, the irregular dark area and folded bright area stands for the BTO and ZIS nanosheets, respectively. Besides, the image shows the close face-to-face contact between BTO and ZIS, indicating the fabrication of 2D/2D interface structure. The fringe distances of 0.263 nm and 0.329 nm are ascribed to (191) plane of BTO and (012) plane of ZIS, respectively (Fig. 3c) (Li et al., 2022a, 2022f; Liu et al., 2020). The above analysis implied that ZIS nanosheets are successfully grown on the surface of BTO to form the 2D/2D ZIS/BTO heterojunction, which would facilitate charge transfer and improve the separation efficiency of photogenerated carriers.

3.2. Composition analysis and properties

The pore structure and specific surface area of samples are investigated by N_2 adsorption/desorption isotherms. As shown in Fig. 4a, all the as-prepared samples show typical type IV isotherms together with a H_3 hysteresis ring. The pore size distributions of $3-10$ nm further demonstrate their mesoporous structures (Fig. 4b) (Bai et al., 2022). Notably, the mesoporous structures can improve mass transfer process and facilitate the separation of photogenerated carriers (Zhou et al., 2011). In addition, the specific surface area and pore volume data are shown in Table S1, the specific surface area of ZIS/BTO is significantly higher than that of BTO, indicating that the introduction of ZIS to the BTO surface has a positive effect on improving the specific surface area, which can expose more adsorption active sites, reduce the migration distance of carriers and promote the activity of the catalysts.

The XRD patterns of the BTO, ZIS, and as-prepared ZIS/BTO heterojunctions are presented in Fig. 5a. The characteristic peaks of BTO can be corresponded and indexed on the $Bi_4Ti_3O_{12}$ (JCPDS No. 35–0795) (Liu et al., 2020). The characteristic peaks of 21.6° and 27.7° are well-matched with the (006) and (102) crystalline planes of $ZnIn_2S_4$ (JCPDS No. 65–2023) (Wang et al., 2021). The typical diffraction peaks of BTO and ZIS can be observed in the prepared ZIS/BTO heterojunction

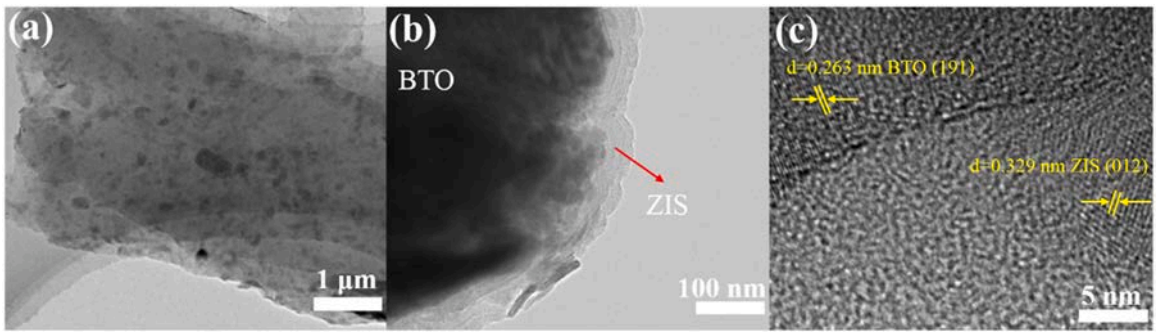

Fig. 3. TEM images of (a-b) ZIS/BTO and (c) HRTEM image.

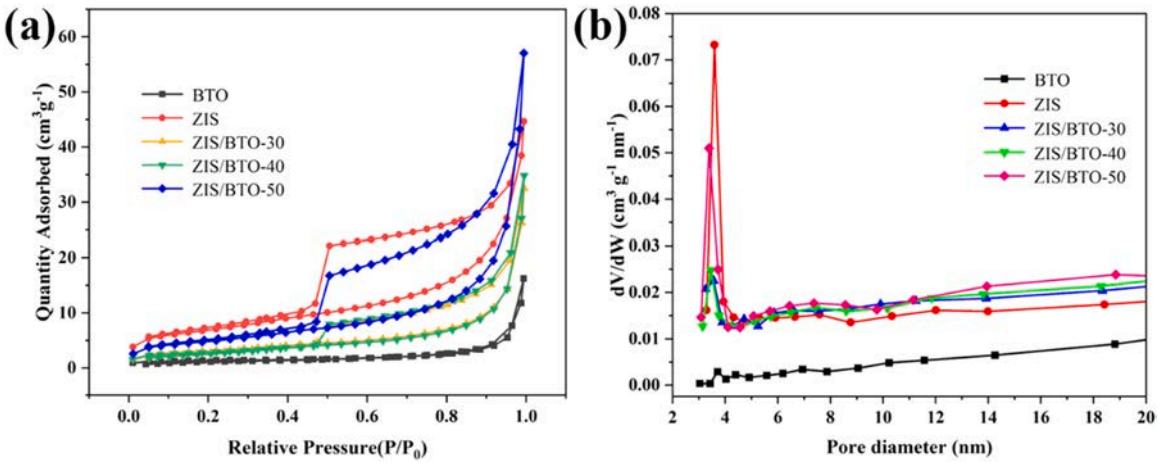

Fig. 4. (a) The N_2 adsorption-desorption isotherm and (b) pore size distributions of all samples.

without other impurity peaks. Besides, with the decline of ZIS content, the intensities of (102) and (006) crystalline planes decreased gradually. The analysis results of the XRD pattern indicate that the ZIS/BTO heterojunctions are successfully synthesized. The ICP-OES is selected to investigate the exact loading amount of ZIS. The obtained contents of elemental Zn and In are 1.82 and 6.98 mg/L, respectively, which are similar to the adding ratio of Zn^{2+} and In^{3+}.

The valence states and surface chemical composition of ZIS/BTO heterojunction can be acquired by XPS. The survey spectrum shows that Zn, In, S, Bi, Ti, and O elements are present in the ZIS/BTO heterojunction (Fig. 5b). In Fig. 5c, two strong peaks located at 164.3 eV and 159.1 eV are matched to the Bi 4 $f_{5/2}$ and Bi 2 $f_{7/2}$, indicating the existence of Bi^{3+} in the composite. As shown in Fig. 5d, the binding energies of 456.06 eV and 462.8 eV are related to Ti $2p_{1/2}$ and Ti $2p_{3/2}$, while the binding energy of 465.88 eV is assigned to the Bi $4d_{3/2}$, which can be attributed to Ti^{4+} and Bi^{3+}. Three peaks with the different oxygen components can be attributed to O 1 s (Fig. 5e). The peak at 528.4 eV and 528.9 eV are ascribed to Bi–O bond and Ti–O bond, respectively. Particularly, the smaller peak located at 530.58 eV can be identified as the adsorbed oxygen on the catalyst surface. Besides, the presence of Zn^{2+} can be confirmed by the peaks at 1021.38 eV and 1044.58 eV, which correspond to Zn $2p_{3/2}$ and Zn $2p_{1/2}$ (Fig. 5f). As shown in Fig. 5g, the two well-defined peaks at 451.5 eV and 444.1 eV correspond to In $3d_{3/2}$ and In $3d_{5/2}$, which can be attributed to In^{3+}. In Fig. 5h, two peaks at 162.2 eV and 161.1 eV are assigned to S $2p_{1/2}$ and S $2p_{3/2}$, respectively, which can be ascribed to S^{2-} in ZIS/BTO heterojunction. The above results are in accordance with the EDS mapping. Additionally, the obvious change in XPS peak position implies that the electron migration occurs at the contact interface between different materials. As shown in Fig. S5, compared to the single sample, the peaks of BTO move to the positive binding energy direction, as well as the peak of ZIS shifts to the negative binding energy direction, when forming the heterojunction. Hence, the formation of the internal electric field between ZIS and BTO can be verified by the change of binding energy. Meanwhile, the Raman spectra of the BTO, ZIS, and as-prepared ZIS/BTO heterojunction are investigated and discussed in the Supporting Information.

3.3. The optical-electrical properties

The UV–vis diffuse reflectance spectroscopy (DRS) was performed to investigate the optical properties of samples to evaluate their visible light absorption. In Fig. 6a, BTO exhibited a low visible light absorbance with an absorption edge at 409 nm. Meanwhile, ZIS has a better absorption capacity in the visible light region with an absorption edge at 572 nm. In addition, the light-harvesting capability of composites is enhanced by the introduction of ZIS, and the absorption band edge of the

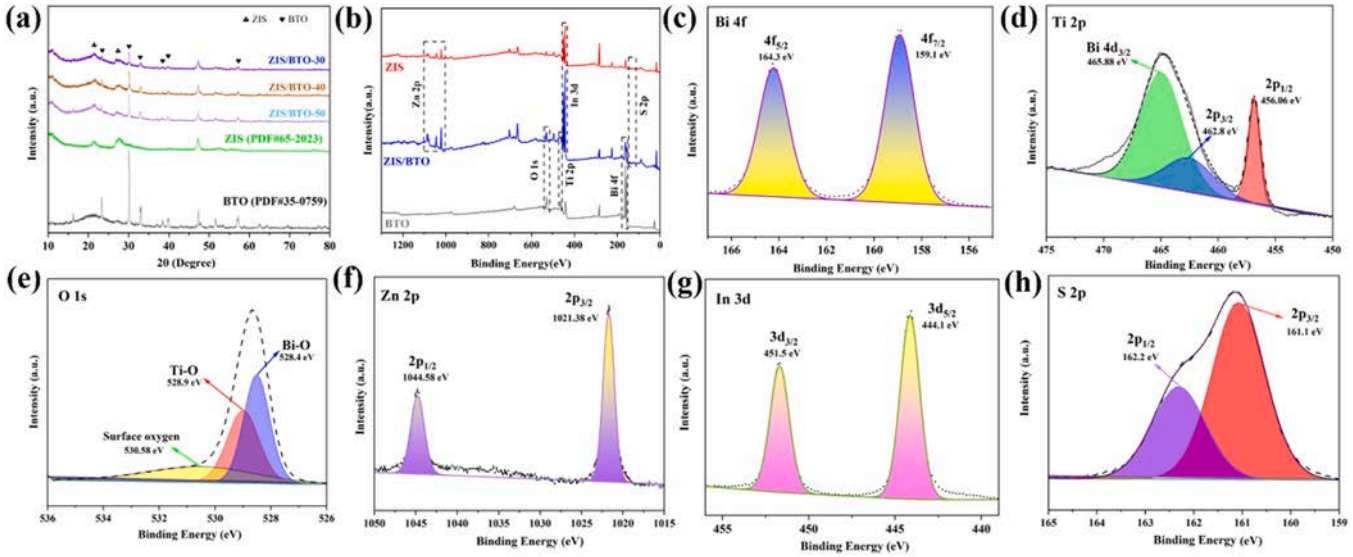

Fig. 5. (a) XRD of the different catalysts, XPS spectrum of (b) ZIS/BTO, (c) Bi 4 f, (d) Ti 2p, (e) O 1 s, (f) Zn 2p, (g) In 3d, and (h) S 2p.

ZIS/BTO-40 is obviously red-shifted compared with pure BTO.

The recombination of photogenerated e^--h^+ impacts the photocatalytic performance of the material. Photoluminescence spectroscopy (PL) can be employed to evaluate the recombination rate of e^--h^+ (Peng et al., 2022). In general, the weaker PL emission intensity means a lower photogenerated e^--h^+ combination rate and higher photocatalytic performance (Wang et al., 2022a). As shown in Fig. 6b, the PL spectra of ZIS, ZIS/BTO-30, ZIS/BTO-40, and ZIS/BTO-50 were investigated when the excitation wavelength is 365 nm. The ZIS performed higher PL emission intensity, which indicated that charge carriers of ZIS are easily combined. After introducing ZIS onto the surface of BTO, the PL emission intensity of composites significantly decreased. Comparatively, ZIS/BTO-40 shows the lowest PL emission intensity. This proves that the synthesis of the composite not only reduces the recombination rate but also effectively promotes the charge carrier migration and prolongs the lifetime of the charge carrier, resulting in the significant enhancement of photocatalytic performance.

To further investigate the photoelectric performance of composite, the separation and migration of photogenerated e^--h^+ in the semiconductors are analyzed by transient photocurrent test and electrochemical impedance spectroscopy (EIS) (Liu et al., 2022b). The generation and migration of e^--h^+ in semiconductors can be reflected by the change of the current density under several cycles of light switching (Guo et al., 2021). As shown in Fig. 6c, BTO exhibits a weak photoelectric signal strength, indicating a faster e^--h^+ recombination rate and lower photocatalytic activity. Moreover, current density of ZIS/BTO-40 is about 2.1 times and 10 times than that of ZIS and BTO, indicating that the fabrication of heterojunction can enhance e^--h^+ generation and migration efficiency. In addition, the smaller impedance arc radius means a lower charge carrier migration resistance, better charge carrier separation rate, and faster migration efficiency. As presented in Fig. 6d, the impedance arc radius decreases with the order of BTO>ZIS>ZIS/BTO-30 >ZIS/BTO-50 >ZIS/BTO-40. In addition, the electrochemical equivalent circuit also exists in Fig. 6d. The existence of heterojunction can be proved based on the improvement of e^--h^+ separation and migration efficiency.

3.4. The photocatalytic degradation performance

The photocatalytic performance of BTO, ZIS, and ZIS/BTO heterojunctions was investigated by the photocatalytic degradation experiment of environmental contaminants. Meanwhile, the optimal weight ratios of ZIS/BTO heterojunctions were also investigated via it. Before visible light irradiation, all samples are placed into TC solution and stirred in the dark environment for half an hour to implement adsorption-desorption equilibrium. The TC removal efficiency of various samples is depicted in Fig. 7a. It can be seen that the adsorption of the BTO is approximately 4.1%. Furthermore, the adsorption of their composites is higher than 38.2%, indicating the synthesis of composites can expose abundant adsorption sites. In the absence of the photocatalyst, the degradation of TC cannot be triggered under visible light irradiation (Fig. S7). The TC removal efficiency by BTO is only 13.2%, indicating the low photocatalytic activity of BTO, which can be ascribed to the rapid recombination of e^--h^+. Noticeably, the TC removal efficiency by ZIS/BTO-40 is 82.1%, which exhibits an attractive removal efficiency compared with other samples. The formation of heterojunction can enhance photocatalytic activity and degradation performance by improving the separation efficiency of photogenerated e^--h^+. In the Supporting Information, the dark experiments (with/without light) are chosen to investigate the effect of adsorption process, and the reasons for

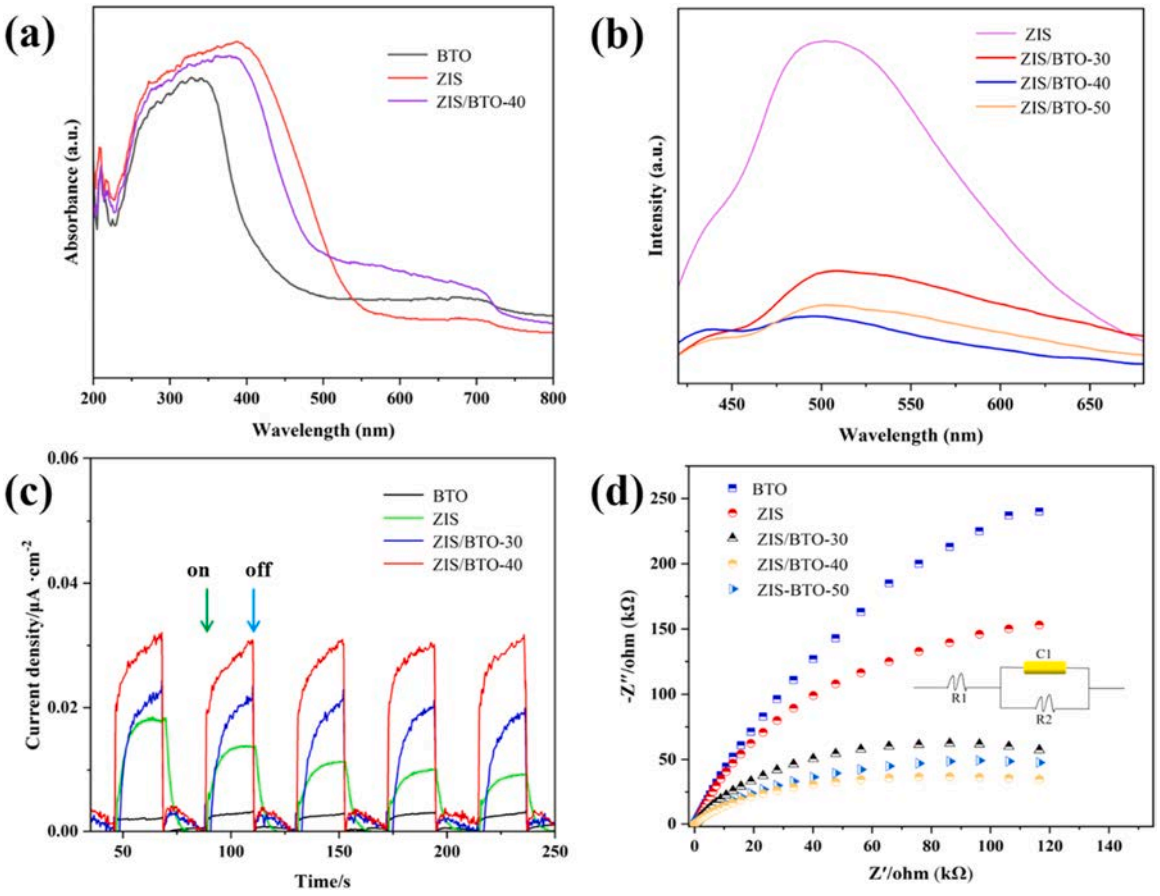

Fig. 6. (a) UV–vis diffuse reflectance spectroscopy, (b) Photoluminescence spectroscopy, (c) Transient photocurrent test, and (d) electrochemical impedance spectroscopy of different photocatalysts.

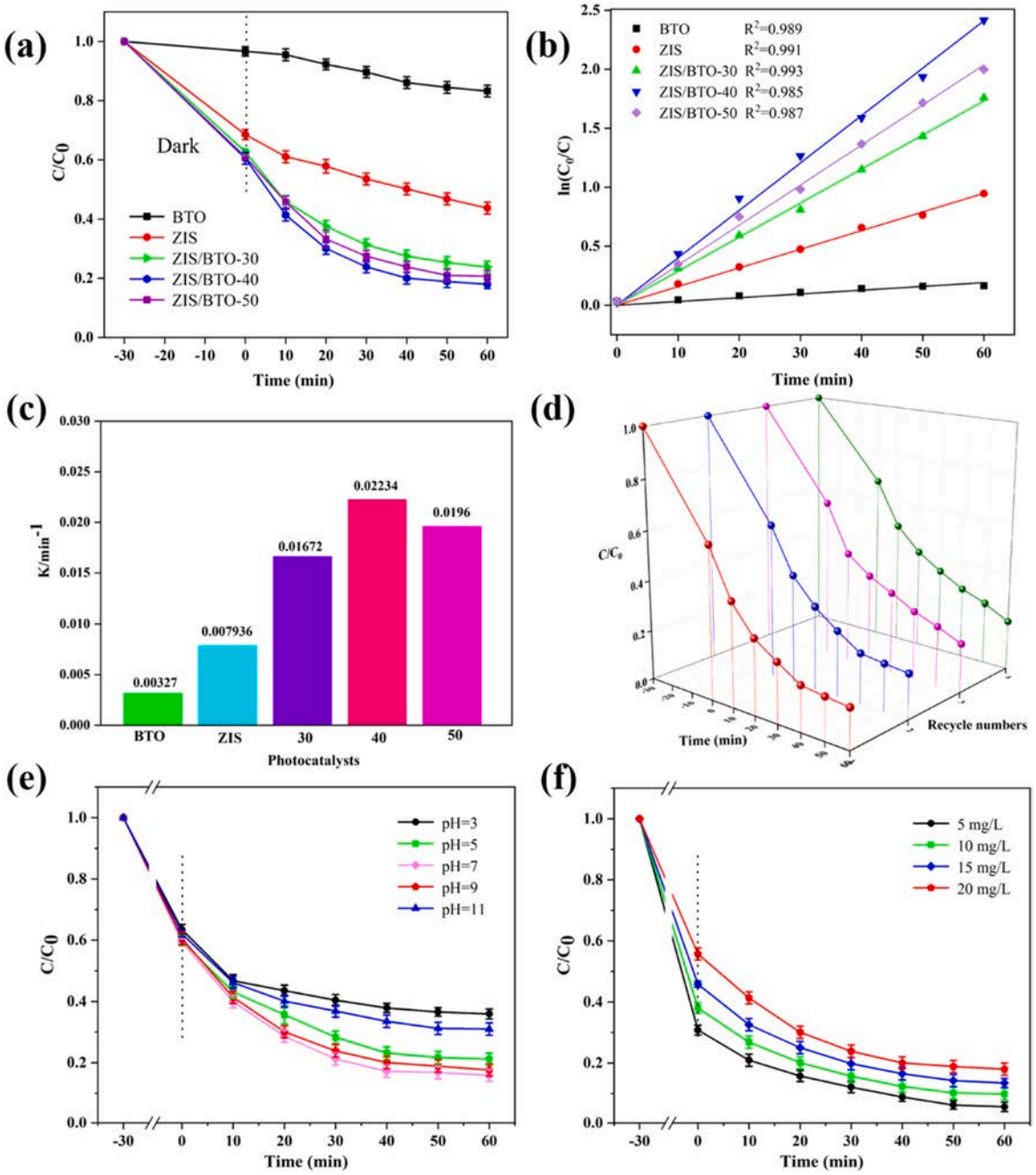

Fig. 7. (a) Removal efficiency of different photocatalysts, (b) corresponding kinetic curve, (c) corresponding rate constants, (d) the cycle test, (e) solution pH, and (f) original TC concentration on the removal efficiency by ZIS/BTO-40.

the high adsorption in the first 30 min are discussed.

Pseudo-first-order kinetic equation ($\ln(C_0/C) = kt$) is selected to describe the rate constant k (min^{-1}) of the TC degradation process (Li et al., 2022b). The linear kinetic curves and rate constant for the TC degradation process by BTO, ZIS, ZIS/BTO-30, ZIS/BTO-40, and ZIS/BTO-50 are displayed in Fig. 7b-c. The degradation rate constant of ZIS is 0.007936 min^{-1}, which can be ascribed to the unsatisfactory recombination of photogenerated e^--h^+. The k constant of ZIS/BTO-30, ZIS/BTO-40 and ZIS/BTO-50 are 0.01672, 0.02234, and 0.0196 min^{-1}, respectively. It is obvious that the k constant of composite is significantly improved. It is worth note that ZIS/BTO-40 has excellent photocatalytic activity, which is up to 6.8 times as much as the ZIS. With the increase of introduction, the active sites of the catalyst surface decrease, resulting in a lower k constant for ZIS/BTO-50. Based on the result of the photocatalytic degradation experiment and the optical-electrical properties test, the optimal BTO weight ratio of the composite is 40%. Notably, compared with other reported photocatalysts (Table S2), the ZIS/BTO-40 exhibits better TC degradation performance.

The reusability of ZIS/BTO-40 is investigated by the consecutive cycle tests. As shown in Fig. 7d, the TC removal efficiency remained stable above 78.1% after four consecutive cycles without significant deactivation. Meanwhile, no obvious changes are founded in XRD patterns of fresh and used ZIS/BTO-40 samples (Fig. S9), indicating that ZIS/BTO-40 samples are as photocatalytic material has favorable stability and reusability. The TC degradation performance of ZIS/BTO-40 in real water environment is also investigated in the Supporting Information.

Generally, the environment pH has a significant effect on the pollutant photodegradation process, which influences the generation of

active species (Li et al., 2022c, 2022d, 2022e). The photocatalytic degradation performance at different pH conditions is evaluated. As shown in Fig. 7e, with the increase in pH, the TC removal efficiency gradually increased, and the maximum removal efficiency is obtained at the pH of 7, reaching about 80.1%. This result can be ascribed that the process of protonation and deprotonation of active species are not realized under acidic conditions, restricting the generation of $\bullet O_2^-$. Under strong alkaline conditions, the •OH could be consumed due to the reaction process between •OH and excess OH^-. The above results show that ZIS/BTO has a good TC removal efficiency in a solution environment from the pH of 5–9.

In Fig. 7f, the effect of initial pollutant concentration on the photodegradation process is investigated. The results showed that the pollutant concentration is comparatively low at 5 mg/L, and the TC removal efficiency is about 95.2%. But, when the pollutant concentration is increased to 10, 15, and 20 mg/L, the removal efficiency is decreased significantly to 89.1%, 86.2%, and 80.3%, respectively. With the increase of the initial TC concentration, the adsorption value and removal efficiency of pollutants by the photocatalysts changed significantly. It can be considered that the limited active sites and constant photo-excited active species of photocatalysts are difficult to match with more intensive adsorption and degradation reaction of increasing pollutant concentrations. In addition, the mineralization rate is evaluated by total organic carbon (TOC) analysis. In Fig. S11, the TOC removal efficiency follows the same trend as the photo-degradation process.

The possible degradation pathways are analyzed by HPLC-MS. As shown in Fig. 8, the two intermediates of P1 (*m/z* of 428) and P2 (*m/z* of 462) are obtained by the reaction of oxidation and hydroxylation, respectively. The intermediates of P3 and P4 (*m/z* of 365 and 264) are produced by the further catalyzed through deamination and demethylation reaction. Subsequently, P5 (*m/z* of 88) is formed via the ring-opening reaction. On the other hand, P2 is further decomposed. Two intermediates P6 and P7 (*m/z* of 322 and 349) are generated via hydroxylation and demethylation reaction and are further oxidized to smaller intermediates of P8 (*m/z* of 279). Besides, the intermediate P9 (*m/z* of 149) is obtained via further ring-opening reactions.

The toxicity assessment of TC and degradation intermediates are analyzed by Toxicity Estimation Software Tool (T.E.S.T). The acute toxicity (Daphnia magna LC50), developmental toxicity, and mutagenicity can be illustrated by the quantitative structure-activity relationship (Li et al., 2022c, 2022d, 2022e). The detailed description of toxicity assessment by T.E.S.T is discussed in the Supporting Information. As shown in Fig. 9**a**, the median lethal dose (LC50) of TC in Daphnia magna is 0.48 mg/L, which is regarded as a "very toxic" level. The LC50 values of the degradation intermediates greatly increased and can be classified into three grades "toxic", "harmful" and "not harmful", indicating that the acute toxicity is significantly reduced after photocatalytic degradation. Moreover, TC is a mutagenicity positive chemical (Fig. 9b), while the mutagenicity of all the degradation intermediates (excluding P1, P2, and P6) declined, especially P4, P5, P8, and P9 are mutagenicity negative. As shown in Fig. 9c, the developmental toxicity of degradation intermediates is also greatly lower than that of TC. Based on the above result, the photocatalytic process can effectively attenuate the toxicity of TC.

3.5. Possible photocatalytic degradation mechanism

The roles of active oxygen species are explored in the photocatalytic degradation of organic pollutants. AO, BQ, and IPA are selected as the scavengers to trap h^+, $\bullet O_2^-$, and •OH for the degradation reaction, respectively (Chen et al., 2022b). As shown in Fig. 10a, the TC degradation efficiency is 82.46% without any radical scavenger. Among them, when AO and IPA are introduced into the reaction system, the TC removal efficiency decrease to 69.8% and 74.6%, respectively, indicating that •OH and h^+ have inhibitory effects during photocatalytic processes. Moreover, the TC degradation efficiency decreased from 82.46% to 55.1% in the presence of BQ, indicating that $\bullet O_2^-$ plays an essential role in the degradation reaction system. The presence of $\bullet O_2^-$ and •OH can also be verified by the variation of trapping agent concentrations in the Supporting Information.

The existence of $\bullet O_2^-$ and •OH in the photocatalysis process is further explored by ESR spectra. As shown in Fig. 10b-c, the signal of radicals cannot be detected under dark conditions. The signal of $\bullet O_2^-$ and •OH can be observed clearly after light irradiation for 10 min. A four-characteristic signal (ratio of 1:2:2:1) and a four unique signal (ratio of 1:1:1:1) are detected, which represent the existence of •OH and $\bullet O_2^-$, respectively. This result is the same as the result of the trapping experiment, which confirms the existence of radicals.

To investigate the possible photocatalytic degradation mechanism, the Tauc plots, Mott−Schottky (M-S) plots, and XPS valence band spectra are selected to analyze the energy band structure of BTO and ZIS. The bandgap energy (Eg) is obtained by Tauc plots based on DRS. The Tauc plots are drawn according to the formula of $(\alpha h\nu)^{1/2}=A(h\nu-Eg)$,

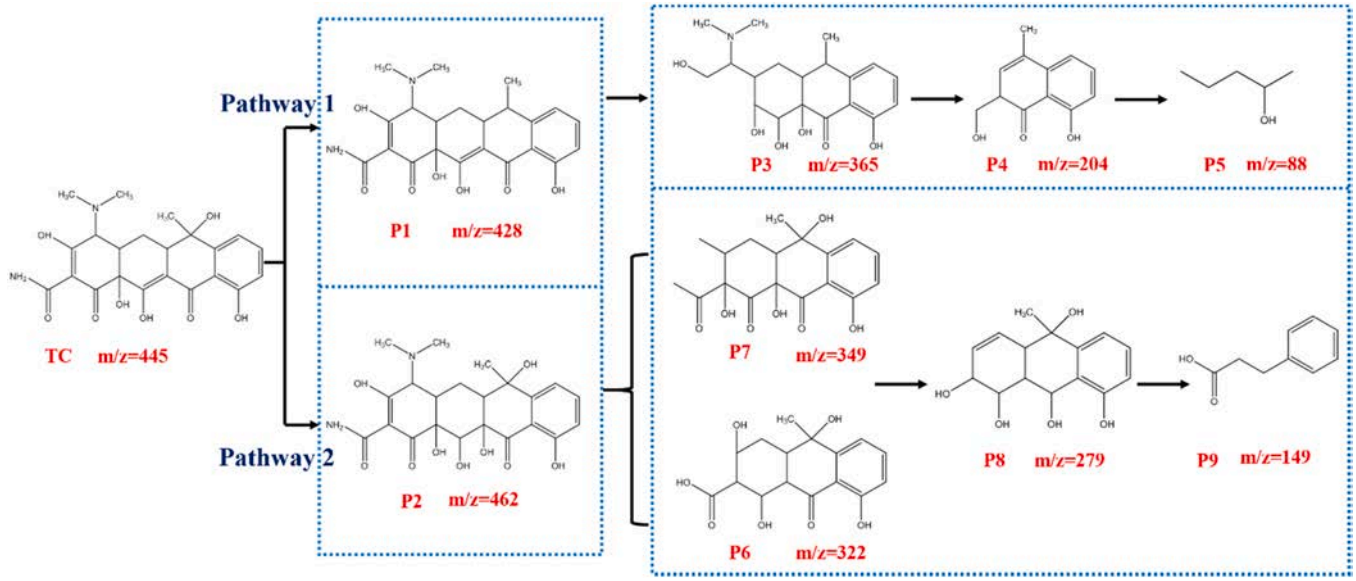

Fig. 8. Proposed photocatalytic degradation pathways.

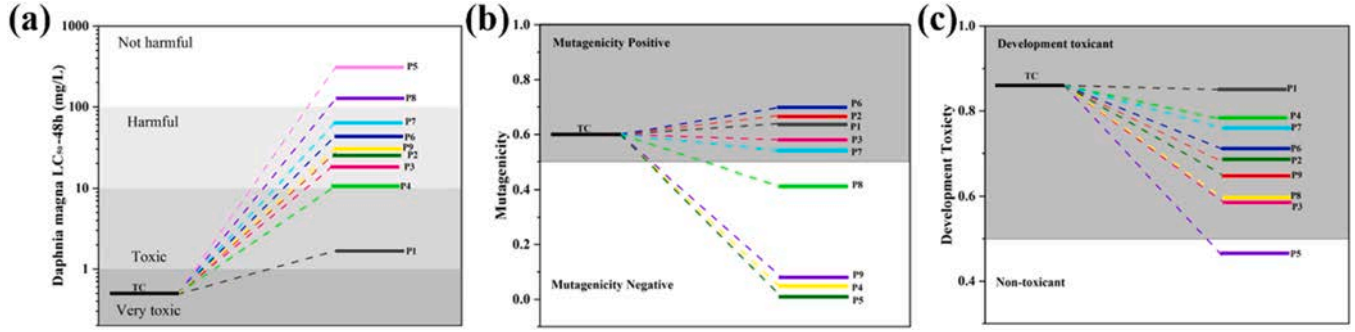

Fig. 9. Toxicity analysis of TC and intermediates: (a) Daphnia magna LC50, (b) mutagenicity, and (c) Developmental toxicity.

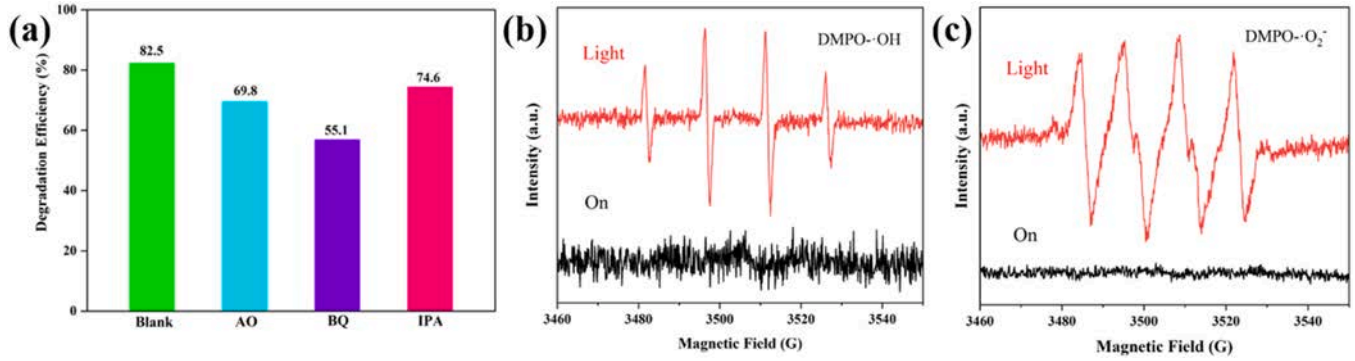

Fig. 10. (a) The trapping experiments of the degradation process, (b)(c) ESR spectra analysis of •OH and $•O_2^-$.

where α represents the absorption coefficient and $h\nu$ is the photon energy. As shown in Fig. 11a, the Eg of BTO and ZIS are about 2.87 eV and 2.25 eV, respectively. The flat-band potential (E_{fb}) of semiconductor photocatalysis can be explained and evaluated by the M-S plots. In Fig. 11b-c and Fig. S13, both BTO and ZIS have positive slopes, indicating that they are n-type semiconductors (Liang et al., 2021). Based on

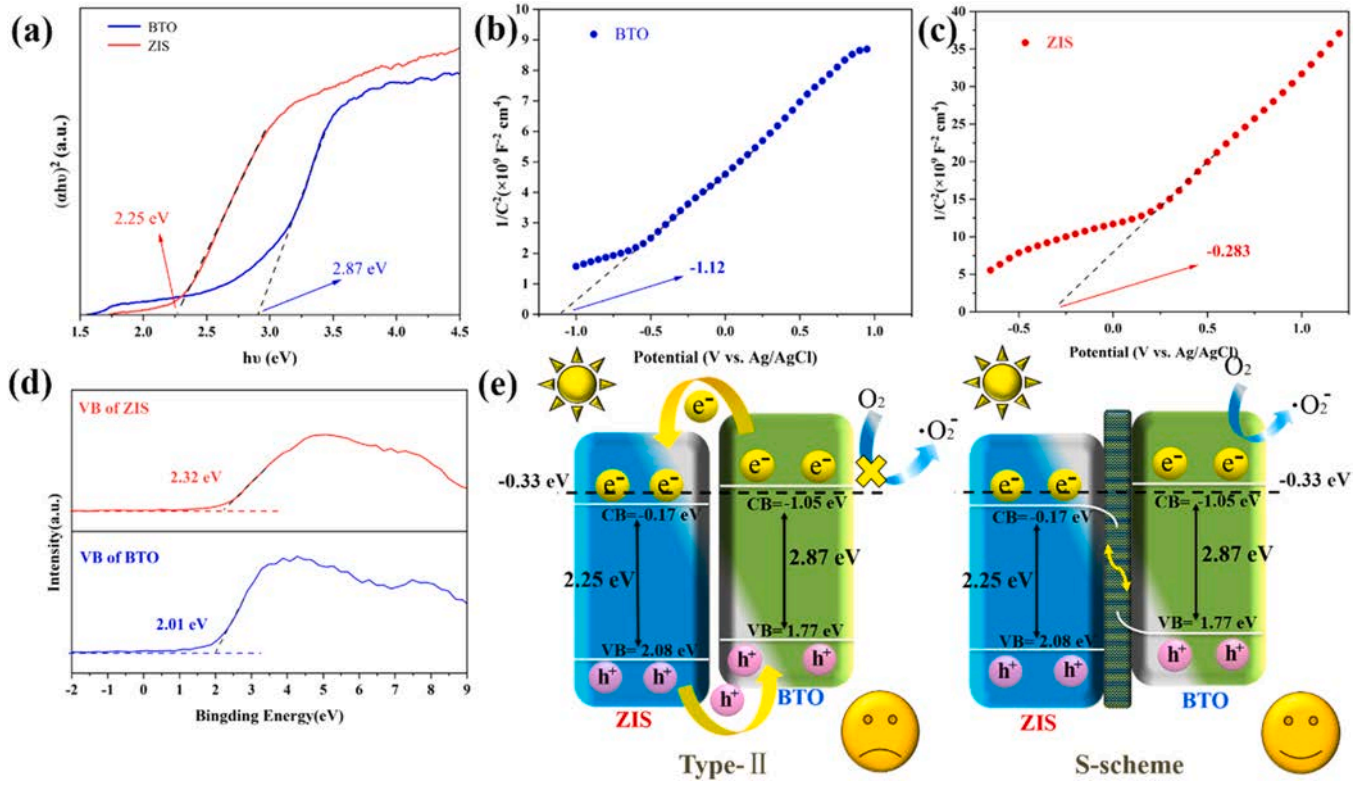

Fig. 11. (a) The bandgap energy, (b)(c) Mott−Schottky plots, (d) VB-XPS, and (e) band structure of different samples.

the intercept of curve tangent, the E_{fb} of BTO and ZIS are obtained as − 1.12 eV and − 0.28 eV, respectively. The above results are obtained versus Ag/AgCl (vs Ag/AgCl) as the reference electrode, which needs to be revised to the result of versus normal hydrogen electrode (vs NHE) (Yang et al., 2021). According to the formula of $E_{NHE} = E_{Ag/AgCl} + 0.197$, the E_{fb} of BTO and ZIS are calculated as − 0.923 eV and − 0.086 eV, respectively. In general, the conduction band positions (CB) of n-type semiconductor is about 0.1 eV lower than E_{fb} (Bai et al., 2022; Wang et al., 2021). Therefore, the E_{CB} of BTO and ZIS are calculated as − 1 eV and − 0.19 eV, respectively. Furthermore, the valence band positions are evaluated by XPS valence band spectra. In Fig. 11d, the $E_{VB,\ XPS}$ of BTO and ZIS are approximately 2.01 eV and 2.32 eV, respectively. Besides, the value of actual E_{VB} will be skewed by the contact potential difference. Hence, $E_{VB,\ XPS}$ should be revised based on the formula $E_{VB,\ NHE} = \phi + E_{VB,\ XPS} - 4.44$, here ϕ and $E_{VB,\ NHE}$ represent the work function of the test instrument (ϕ = 4.2 eV), and the valence band position of the versus normal hydrogen electrode, respectively (Wang et al., 2020). The $E_{VB,\ NHE}$ of BTO and ZIS are calculated as 1.77 eV and 2.08 eV, respectively. In addition, E_{CB} of BTO and ZIS can be calculated by $E_{CB} = E_{VB} - Eg$. The E_{CB} of BTO and ZIS are obtained as − 1.05 eV and − 0.17 eV, respectively, which are similar to the result of E_{CB} by M-S plots. And the results are employed to analyze the possible charge transfer mechanism.

In Fig. 11e, the charge transfer of the ZIS/BTO heterojunction may follow the type-II heterojunction or S-scheme heterojunction, due to the staggered energy structure. If the sample is a traditional type-II heterojunction, the photogenerated carriers are generated by the sample under the visible light. The e^- can be transferred from the BTO to ZIS and accumulated in the CB of ZIS, the h^+ can be transferred from the ZIS to BTO and accumulated in the VB of BTO. Notably, the CB potential of ZIS is lower than the potential of $O_2/\cdot O_2^-$ (−0.33 eV) (Chen et al., 2022a; Chen et al., 2022b). The dissolved oxygen cannot be reduced to $\cdot O_2^-$ by the e^- in the CB of ZIS. It is worth noting that the presence of $\cdot O_2^-$ in the photocatalytic process is confirmed by ESR and trapping experiment. According to the analysis above, the charge transfer mechanism of the sample cannot follow the type-II heterojunction. Therefore, the photogenerated carrier transfer mechanism of the sample is suitable for the S-scheme heterojunction, rather than type-II heterojunction.

The work function (ϕ) is an important parameter of catalytic materials, which affects the direction of electron transport between the material interfaces (Chen, N. et al., 2022). Typically, the value of ϕ can be calculated by the binding energy of the secondary cutoff edge of the UPS curve (Li et al., 2022a). Especially, the position of the Fermi energy level can be evaluated by the formula follows: $\phi = E_{VAC} - E_F$, where E_{VAC} and E_F represent the potential of vacuum level and Fermi energy level, respectively. Theoretically, the electron rearrangement can be occurred bring E_F into equilibrium when two materials come into contact with each other (Wang et al., 2021).

As shown in Fig. 12a-b, the BTO has a lower ϕ (4.37 eV) compared with the ϕ of ZIS (6.79 eV). It can be considered that the electrons should

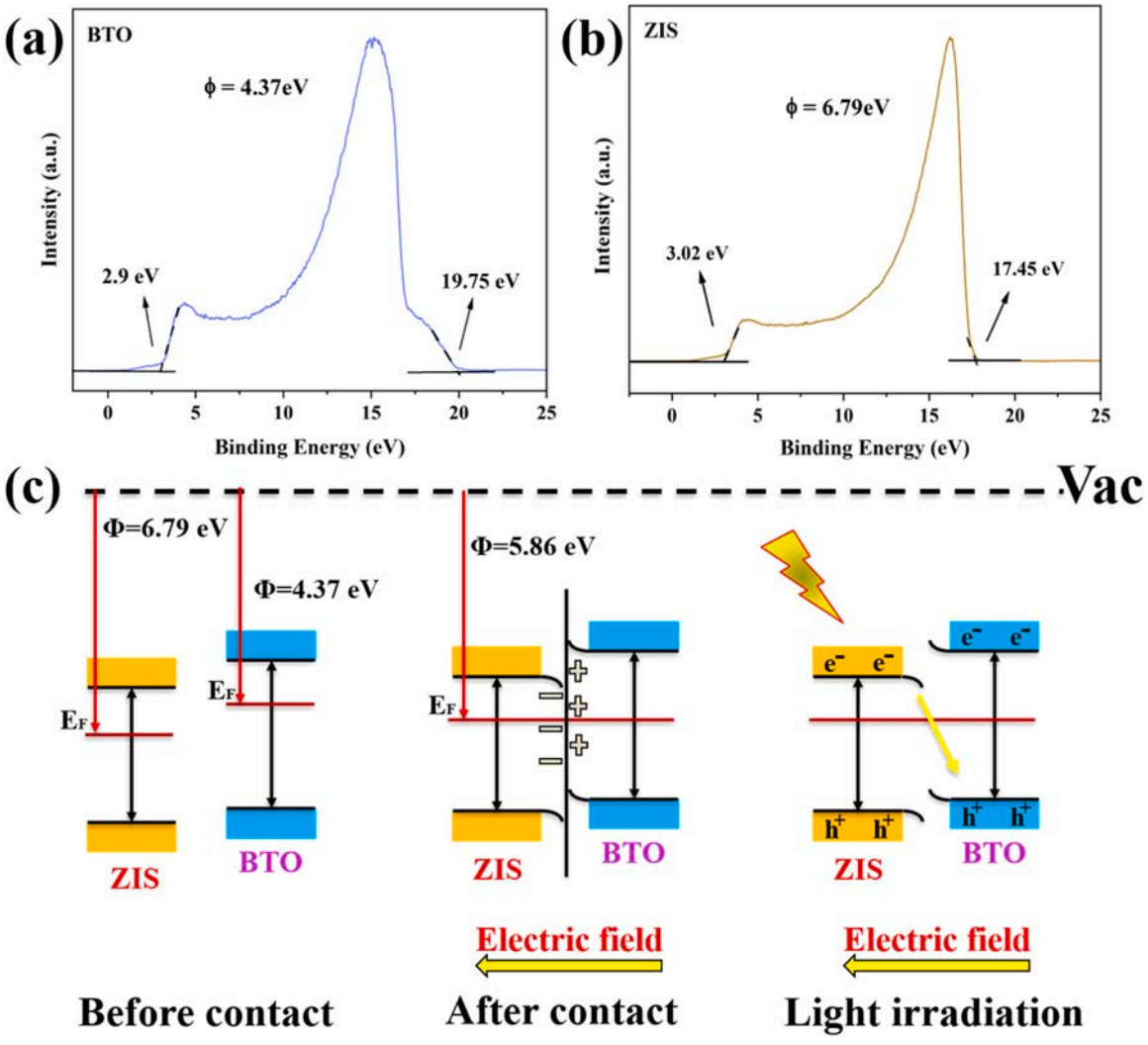

Fig. 12. (a)(b) UPS of different samples and (c) charge transfer mechanism.

be transferred from the BTO side to ZIS until the balance of E_F is reached due to the electron always transferred from the low ϕ to the high ϕ (Fig. 12c). Meanwhile, a new thermodynamic equilibrium is established again. The electron depletion layer will be formed gradually around BTO and the electron accumulation layer will be formed gradually around ZIS, during the transportation of electrons. A built IEF will be established between BTO and ZIS due to the difference in potential, which further facilitate the transportation of electrons from BTO to ZIS and accordance with the aforementioned result of XPS. At the same time, the E_F of BTO and ZIS can be aligned at the same potential (ϕ = 5.86 eV, as shown in Fig. S14), which causes band bending of the semiconductor. Simply, the VB of BTO bends upward and the CB of ZIS bends downward. Under visible light irradiation, the e^- of BTO and ZIS are excited from VB to CB. The e^- in the CB of ZIS and the h^+ in the VB of BTO are induced to recombine based on the presence of IEF, which will prevent the recombination of h^+ and e^- in ZIS and BTO. Furthermore, the occurrence of band bending is beneficial to the supply and acquisition of photoelectrons, which guarantees the transportation of electrons and weakens the energy barrier. The S-scheme heterojunction recombines the meaningless e^- in the CB of ZIS and the h^+ in the VB of BTO and retains useful h^+ and e^- in ZIS and BTO. Therefore, the charge transfer mechanism of the S-scheme heterojunction endows the ZIS/BTO with higher redox capacity to degrade TC.

4. Conclusion

In summary, 2D/2D ZIS/BTO S-scheme heterojunction is constructed via a low-temperature solvothermal method, and the ZIS nanosheets are uniformly distributed on the BTO surface. The obtained 2D/2D ZIS/BTO S-scheme heterojunction exhibits excellent photocatalytic activity, which can be attributed to the abundant active sites and efficient photogenerated carrier migration and separation capability. Correspondingly, the ZIS/BTO-40 exhibits favorable TC removal efficiency with a rate constant of 0.023 min^{-1}, which is 6.8 times better than that of pristine ZIS. Furthermore, the excellent reusability and stability of ZIS/BTO-40 is confirmed by the cycling test. Moreover, the results of trapping experiment and ESR indicated that the S-scheme heterojunction is a reasonable inference to explain the photogenerated carrier transfer mechanism. Notably, the work function calculations reveal that built-IEF and band bending at the contact interface of heterojunctions are essential for enhancing catalytic activity. This work offers an effective strategy to fabricate S-scheme heterojunction photocatalysts, which shows a promising perspective in the field of organic pollutant remediation.

Environmental implication

Tetracycline hydrochloride (TC), a typical antibiotic medicine, has been widely used in aquaculture and animal husbandry. Inevitably, TC tends to be discharged into the aquatic ecosystem owing to its poor biodegradability and higher water solubility, thereby posing a potential threat to human drinking water safety and ecosystem balance. The synthesized ZIS/BTO heterojunction photocatalysts have favorable catalytic activity and can be used to achieve efficient degradation of TC in wastewater. Notably, the toxicity assessment of TC and degradation intermediates by the Toxicity Estimation Software Tool demonstrate that the degradation process can significantly attenuate the toxicity and mutagenicity of TC.

CRediT authorship contribution statement

Qi Zhou: Conceptualization, Methodology, Software, Validation, Formal analysis, Investigation, Resources, Data curation, Writing – original draft, Writing – review & editing, Visualization, Supervision, Project administration. **Luhong Zhang:** Validation, Supervision, Project administration, Funding acquisition, Project administration. Longfei Zhang: Validation, Writing – review & editing, Supervision. **Bin Jiang:** Validation, Writing – review & editing, Supervision. **Yongli Sun:** Validation, Supervision, Project administration, Funding acquisition, Project administration.

Declaration of Competing Interest

The authors declare that they have no known competing financial interests or personal relationships that could have appeared to influence the work reported in this paper.

Data availability

Data will be made available on request.

Acknowledgements

We would like to thank the researchers in the Shiyanjia Lab (www.shiyanjia.com) for their helping with BET, UPS and ESR test.

Appendix A. Supporting information

Supplementary data associated with this article can be found in the online version at doi:10.1016/j.jhazmat.2022.129438.

References

Bai, J., Shen, R., Jiang, Z., Zhang, P., Li, Y., Li, X., 2022. Integration of 2D layered CdS/WO3 S-scheme heterojunctions and metallic Ti3C2 MXene-based Ohmic junctions for effective photocatalytic H2 generation. Chin. J. Catal. 43 (2), 359–369. https://doi.org/10.1016/s1872-2067(21)63883-4.

Chen, N., Jia, X., He, H., Lin, H., Guo, M., Cao, J., Zhang, J., Chen, S., 2022. Promoting photocarriers separation in S-scheme system with Ni2P electron bridge: the case study of BiOBr/Ni2P/g-C3N4. Chin. J. Catal. 43 (2), 276–287. https://doi.org/10.1016/s1872-2067(21)63817-2.

Chen, Z., Li, Y., Tian, F., Chen, X., Wu, Z., 2022. Synthesis of BiVO4/g-C3N4 S-scheme heterojunction via a rapid and green microwave route for efficient removal of glyphosate. Sep. Purif. Technol. 287 https://doi.org/10.1016/j.seppur.2022.120507.

Dai, B., Chen, X., Yang, X., Yang, G., Li, S., Zhang, L., Mu, F., Zhao, W., Leung, D.Y.C., 2022. Designing S-scheme Au/g-C3N4/BiO1.2I0.6 plasmonic heterojunction for efficient visible-light photocatalysis. Sep. Purif. Technol. 287 https://doi.org/10.1016/j.seppur.2022.120531.

Dou, X., Zhang, C., Shi, H., 2022. The simultaneous promotion of Cr (VI) photoreduction and tetracycline removal over 3D/2D Cu2O/BiOBr S-scheme nanostructures. Sep. Purif. Technol. 282 https://doi.org/10.1016/j.seppur.2021.120023.

Fan, H.-T., Wu, Z., Liu, K.-C., Liu, W.-S., 2022. Fabrication of 3D CuS@ZnIn2S4 hierarchical nanocages with 2D/2D nanosheet subunits p-n heterojunctions for improved photocatalytic hydrogen evolution. Chem. Eng. J. 433, 134474 https://doi.org/10.1016/j.cej.2021.134474.

Guo, X., Liu, Y., Yang, Y., Mu, Z., Wang, Y., Zhang, S., Wang, S., Hu, Y., Liu, Z., 2021. Effective visible-light excited charge separation in all-solid-state Ag bridged BiVO4/ZnIn2S4 core-shell structure Z-scheme nanocomposites for boosting photocatalytic organics degradation. J. Alloy. Compd. 887 https://doi.org/10.1016/j.jallcom.2021.161389.

Jiang, Y., Huang, K., Ling, W., Wei, X., Wang, Y., Wang, J., 2021. Investigation of the kinetics and reaction mechanism for photodegradation tetracycline antibiotics over sulfur-doped Bi2WO6-x/ZnIn2S4 Direct Z-scheme heterojunction. Nanomaterials 11 (8). https://doi.org/10.3390/nano11082123.

Jin, Z., Li, J., Liu, D., Sun, Y., Li, X., Cai, Q., Ding, H., Gui, J., 2022. Effective promotion of spacial charge separation of dual S-scheme (1D/2D/0D) WO3@ZnIn2S4/Bi2S3 heterojunctions for enhanced photocatalytic performance under visible light. Sep. Purif. Technol. 284 https://doi.org/10.1016/j.seppur.2021.120207.

Koutavarapu, R., Reddy, C.V., Syed, K., Reddy, K.R., Saleh, T.A., Lee, D.Y., Shim, J., Aminabhavi, T.M., 2022. Novel Z-scheme binary zinc tungsten oxide/nickel ferrite nanohybrids for photocatalytic reduction of chromium (Cr (VI)), photoelectrochemical water splitting and degradation of toxic organic pollutants. J. Hazard Mater. 423 (Pt A), 127044 https://doi.org/10.1016/j.jhazmat.2021.127044.

Li, L., Ma, D., Xu, Q., Huang, S., 2022. Constructing hierarchical ZnIn2S4/g-C3N4 S-scheme heterojunction for boosted CO_2 photoreduction performance. Chem. Eng. J. 437. https://doi.org/10.1016/j.cej.2022.135153.

Li, M., Li, P., Zhang, L., Chen, M., Tang, J., Qin, C., Ling Jie Lee, S., Lin, S., 2022. Facile fabrication of ZnO decorated ZnFe-layered double hydroxides @ biochar nanocomposites for synergistic photodegradation of tetracycline under visible light. Chem. Eng. J. 434 https://doi.org/10.1016/j.cej.2022.134772.

Li, X., Luo, Q., Han, L., Deng, F., Yang, Y., Dong, F., 2022. Enhanced photocatalytic degradation and H2 evolution performance of N CDs/S-C3N4 S-scheme

heterojunction constructed by π-π conjugate self-assembly. J. Mater. Sci. Technol. 114, 222–232. https://doi.org/10.1016/j.jmst.2021.10.030.
Li, X., Qiu, Y., Zhu, Z., Chen, T., Zhang, H., Yin, D., 2022. Construction of magnetically separable dual Z-scheme g-C3N4/α-Fe2O3/Bi3TaO7 photocatalyst for effective degradation of ciprofloxacin under visible light. Chem. Eng. J. 440 https://doi.org/10.1016/j.cej.2022.135840.
Li, X., Yang, Z., Wu, G., Huang, Y., Zheng, Z., Garces, H.F., Yan, K., 2022. Fabrication of ultrathin lily-like NiCo2O4 nanosheets via mooring NiCo bimetallic oxide on waste biomass-derived carbon for highly efficient removal of phenolic pollutants. Chem. Eng. J. 441 https://doi.org/10.1016/j.cej.2022.136066.
Li, Y., Yu, B., Hu, Z., Wang, H., 2022. Construction of direct Z-scheme SnS2@ZnIn2S4@kaolinite heterostructure photocatalyst for efficient photocatalytic degradation of tetracycline hydrochloride. Chem. Eng. J. 429 https://doi.org/10.1016/j.cej.2021.132105.
Lian, X., Chen, S., He, F., Dong, S., Liu, E., Li, H., Xu, K., 2022. Photocatalytic degradation of ammonium dinitramide over novel S-scheme g-C3N4/BiOBr heterostructure nanosheets. Sep. Purif. Technol. 286 https://doi.org/10.1016/j.seppur.2022.120449.
Liang, Y., Xu, W., Fang, J., Liu, Z., Chen, D., Pan, T., Yu, Y., Fang, Z., 2021. Highly dispersed bismuth oxide quantum dots/graphite carbon nitride nanosheets heterojunctions for visible light photocatalytic redox degradation of environmental pollutants. Appl. Catal. B: Environ. 295 https://doi.org/10.1016/j.apcatb.2021.120279.
Liu, C., Xu, J., Niu, J., Chen, M., Zhou, Y., 2020. Direct Z-scheme Ag3PO4/Bi4Ti3O12 heterojunction with enhanced photocatalytic performance for sulfamethoxazole degradation. Sep. Purif. Technol. 241 https://doi.org/10.1016/j.seppur.2020.116622.
Liu, H., Chen, J., Guo, W., Xu, Q., Min, Y., 2022. A high efficiency water hydrogen production method based on CdS/WN composite photocatalytic. J. Colloid Interface Sci. 613, 652–660. https://doi.org/10.1016/j.jcis.2022.01.014.
Liu, K., Zhang, H., Fu, T., Wang, L., Tang, R., Tong, Z., Huang, X., 2022. Construction of BiOBr/Ti3C2/exfoliated montmorillonite Schottky junction: New insights into exfoliated montmorillonite for inducing MXene oxygen functionalization and enhancing photocatalytic activity. Chem. Eng. J. 438 https://doi.org/10.1016/j.cej.2022.135609.
Mu, F., Dai, B., Wu, Y., Yang, G., Li, S., Zhang, L., Xu, J., Liu, Y., Zhao, W., 2022. 2D/3D S-scheme heterojunction of carbon nitride/iodine-deficient bismuth oxyiodide for photocatalytic hydrogen production and bisphenol A degradation. J. Colloid Interface Sci. 612, 722–736. https://doi.org/10.1016/j.jcis.2021.12.196.
Peng, P., Chen, Z., Li, X., Wu, Y., Xia, Y., Duan, A., Wang, D., Yang, Q., 2022. Biomass-derived carbon quantum dots modified Bi2MoO6/Bi2S3 heterojunction for efficient photocatalytic removal of organic pollutants and Cr (Vl). Sep. Purif. Technol. 291 https://doi.org/10.1016/j.seppur.2022.120901.
Tan, M., Ma, Y., Yu, C., Luan, Q., Li, J., Liu, C., Dong, W., Su, Y., Qiao, L., Gao, L., Lu, Q., Bai, Y., 2021. Boosting photocatalytic hydrogen production via interfacial engineering on 2D ultrathin Z-scheme ZnIn2S4/g-C3N4 heterojunction. Adv. Funct. Mater. 32 (14) https://doi.org/10.1002/adfm.202111740.
Wang, A., Ni, J., Wang, W., Wang, X., Liu, D., Zhu, Q., 2022. MOF-derived N-doped ZnO carbon skeleton@hierarchical Bi2MoO6 S-scheme heterojunction for photodegradation of SMX: mechanism, pathways and DFT calculation. J. Hazard Mater. 426, 128106 https://doi.org/10.1016/j.jhazmat.2021.128106.
Wang, C., Li, S., Cai, M., Yan, R., Dong, K., Zhang, J., Liu, Y., 2022. Rationally designed tetra (4-carboxyphenyl) porphyrin/graphene quantum dots/bismuth molybdate Z-scheme heterojunction for tetracycline degradation and Cr(VI) reduction: performance, mechanism, intermediate toxicity appraisement. J. Colloid Interface Sci. 619, 307–321. https://doi.org/10.1016/j.jcis.2022.03.075.
Wang, K., Shao, X., Zhang, K., Wang, J., Wu, X., Wang, H., 2022. 0D/3D Bi3TaO7/ZnIn2S4 heterojunction photocatalyst towards degradation of antibiotics coupled with simultaneous H2 evolution: In situ irradiated XPS investigation and S-scheme mechanism insight. Appl. Surf. Sci. 596 https://doi.org/10.1016/j.apsusc.2022.153444.
Wang, L., Cheng, B., Zhang, L., Yu, J., 2021. In situ irradiated XPS investigation on S-Scheme TiO2 @ZnIn2S4 photocatalyst for efficient photocatalytic CO_2 Reduction. Small 17 (41), e2103447. https://doi.org/10.1002/smll.202103447.
Wang, S., Wang, Y., Zhang, S.L., Zang, S.Q., Lou, X.W.D., 2019. Supporting ultrathin ZnIn2S4 nanosheets on Co/N-doped graphitic carbon nanocages for efficient photocatalytic H2 generation. Adv. Mater. 31 (41), e1903404 https://doi.org/10.1002/adma.201903404.
Wang, X., Wang, Y., Gao, M., Shen, J., Pu, X., Zhang, Z., Lin, H., Wang, X., 2020. BiVO4/Bi4Ti3O12 heterojunction enabling efficient photocatalytic reduction of CO_2 with H2O to CH3OH and CO. Appl. Catal. B: Environ. 270 https://doi.org/10.1016/j.apcatb.2020.118876.
Wang, Y., Zhao, X., Wang, L., Yang, Y., Jiao, L., Wu, Z., Gao, X., Cheng, S., Lin, M., 2022. A novel nano-sized red phosphorus decorated borocarbonitride heterojunction with enhanced photocatalytic performance for tetracycline degradation. Environ. Sci.: Nano. https://doi.org/10.1039/d2en00071g.
Xi, Y., Chen, W., Dong, W., Fan, Z., Wang, K., Shen, Y., Tu, G., Zhong, S., Bai, S., 2021. Engineering an interfacial facet of S-scheme heterojunction for improved photocatalytic hydrogen evolution by modulating the internal electric field. ACS Appl. Mater. Interfaces 13 (33), 39491–39500. https://doi.org/10.1021/acsami.1c11233.
Xu, F., Meng, K., Cao, S., Jiang, C., Chen, T., Xu, J., Yu, J., 2021. Step-by-step mechanism insights into the TiO2/Ce2S3 S-scheme photocatalyst for enhanced aniline production with water as a proton source. ACS Catal. 12 (1), 164–172. https://doi.org/10.1021/acscatal.1c04903.
Yang, C., Zhang, G., Meng, Y., Pan, G., Ni, Z., Xia, S., 2021. Direct Z-scheme CeO2@LDH core-shell heterostructure for photodegradation of Rhodamine B by synergistic persulfate activation. J. Hazard Mater. 408, 124908 https://doi.org/10.1016/j.jhazmat.2020.124908.
Zhang, C., Wang, Y., Zhang, X., Wang, R., Kou, L., Wang, J., Li, R., Fan, C., 2021. Millimeter-level nitrogen modified activated carbon spheres assisted Bi4Ti3O12 composites for bifunctional adsorption/photoreduction of CO_2. Chem. Eng. J. 417 https://doi.org/10.1016/j.cej.2020.128218.
Zhao, X., Chen, J., Zhao, C., Liu, Y., Liang, Q., Zhou, M., Li, Z., Zhou, Y., 2021. Construction ZnIn2S4/Ti3C2 of 2D/2D heterostructures with enhanced visible light photocatalytic activity: a combined experimental and first-principles DFT study. Appl. Surf. Sci. 570 https://doi.org/10.1016/j.apsusc.2021.151183.
Zhou, W., Sun, F., Pan, K., Tian, G., Jiang, B., Ren, Z., Tian, C., Fu, H., 2011. Well-ordered large-pore mesoporous anatase TiO2 with remarkably high thermal stability and improved crystallinity: preparation, characterization, and photocatalytic performance. Adv. Funct. Mater. 21 (10), 1922–1930. https://doi.org/10.1002/adfm.201002535.
Zou, X., Dong, Y., Ke, J., Ge, H., Chen, D., Sun, H., Cui, Y., 2020. Cobalt monoxide/tungsten trioxide p-n heterojunction boosting charge separation for efficient visible-light-driven gaseous toluene degradation. Chem. Eng. J. 400 https://doi.org/10.1016/j.cej.2020.125919.